Maskless photolithography for rapid Organ-on-a-Chip prototyping and microvascular engineering

Kasi, D.G.

Citation

Kasi, D. G. (2025, December 11). *Maskless photolithography for rapid Organ-on-a-Chip prototyping and microvascular engineering*. Retrieved from https://hdl.handle.net/1887/4285618

Abstract

Retinal vasculopathy with cerebral leukoencephalopathy and systemic manifestations (RVCL- S) is a rare autosomal dominant small vessel disorder caused by C-terminus truncating mutations in TREX1, a DNA-specific exonuclease. RVCL-S can serve as a genetic model for small vessel diseases and vascular dementia. It is characterized by vasculopathies in highly vascularized organs including the retina, liver, kidney and brain. Although the exact underlying mechanism causing these pathologies remains to be elucidated; endothelial cell (EC) dysfunction and inflammation appear to contribute to the disease pathalogy. Despite the development of transgenic RVCL-S mouse models, because of likely discrepancies between human and mouse manifestations, there is a need to develop *in vitro* human models of the disease. Human induced pluripotent stem cells (hiPSC) represent an opportunity to explore these differences *in vitro* human models. Here, we generated hiPSCs from an RVCL-S patient (RVCL-S-hiPSCs) and their isogenic, genetically-corrected counterparts to investigate function in RVCL-S-hiPSC-derived ECs (hiPSC-ECs). Genotype, genomic stability, expression of pluripotency markers and spontaneous three germ-lineage differentiation were confirmed in mutant and genetically-corrected RVCL-S hiPSC lines. EC morphology, marker expression, proliferation and barrier function were however, similar in diseased and corrected hiPSC- ECs. These results suggest that uncovering EC defects observed in RVCL-S patients in hiPSC- ECs might require more complex models that also include immune cells or stimulatory cytokines.

Chapter

Characterization of endothelial cell functionality in RVCL-S using patient-derived hiPSCs

Dennis M. Nahon[1,*], Dhanesh G. Kasi[1,*], Francijna E. van den Hil[1], Marga J. Bouma[1], Albert Blanch-Asensio[1], Ruben W.J. van Helden[1], Richard P. Davis[1], Michel D. Ferrari[3], Gisela M. Terwindt[3], Christian Freund[1], Christine L. Mummery[1], Arn M.J.M. van den Maagdenberg[2,3], Valeria V. Orlova[1]

[1]Department of Anatomy and Embryology, Leiden University Medical Center, Leiden, The Netherlands

[2]Department of Human Genetics, Leiden University Medical Center, Leiden, The Netherlands

[3]Department of Neurology, Leiden University Medical Center, Leiden, The Netherlands

*Authors contributed equally

Manuscript in preparation

Introduction

Retinal vasculopathy with cerebral leukoencephalopathy and systemic manifestations (RVCL-S) is a rare, autosomal dominant small vessel disease caused by truncating mutations in the C-terminus of abundantly expressed 3’-5’ DNA exonuclease; TREX1[1]. Patients with this mutation most commonly start developing symptoms related to vasculopathies from 30-50 years of age in multiple, highly vascularized organs such as the retina, brain, liver and kidney. The symptoms are diverse and may include progressive visual impairment, stroke, migraine, cognitive decline, apathy, and pneumonia which often leads to premature death[2,3]. Current treatment options are very limited and focus on alleviating symptoms.

The dysfunctional TREX1 protein in RVCL-S retains its exonuclease function, but truncation of its endoplasmic reticulum (ER)-localization domain results in a disruption of both the ER interaction and localization[1,4,5]. How this change in subcellular localization results in the disease phenotype remains to be elucidated; however, previous work indicated a role of both the endothelium and an auto-inflammation response. Disease hypotheses were strengthened by the discovery of TREX1 expression in microglia in the brain[6] and in ECs of the vasculature[7]. In addition, recent studies seem to have demonstrated that the TREX1 C-terminus is a critical regulator of oligosaccharyltransferase (OST) activity, an enzyme that facilitates N-glycosylation of polypeptides[5]. So in addition to a loss of localization, a truncated TREX1 protein seems to lead to dysregulated OST activity, ultimately generating immunogenic free glycans. The glycans are known to induce expression of pro-inflammatory genes known as IFN-stimulated genes (ISGs)[5]. Regardless of the published findings, OST involvement has to be confirmed by other studies. Another disease hypothesis is built around observed alterations in patient vessels that manifest both structurally as thickening of the vessel wall e.g. multi-laminated basement membranes[8], and functionally, as reduced flow-mediated dilatation responses[9]. Vascular involvement was further confirmed by a study demonstrating elevated levels of the endothelial damage-related markers von Willebrand factor (vWF) and angiopoietin-2 in RVCL-S patients[10].

Notably, the findings were partially supported by genetic RVCL-S mouse models. A mouse model with a knock-in of the human *TREX1* gene carrying the most common V235fs RVCL-S mutation demonstrated increased auto-inflammation by showing a distinct auto-antibody profile[11]. An independent mouse model with a specific knock-in of the same truncation mutation resulted in increased mortality and reduced blood flow and vascular function[12]. Even though homozygous mice were investigated- whereas patients are heterozygous - both mouse models were unable to reproduce the histological abnormalities in various organs or structural abnormalities in the vasculature seen in human patients. Admittedly though, no in-depth characterization was performed that would reveal the abnormalities seen in the patients. A logical complication of recapitulating all pathology seen in humans is the shorter lifespan of the mice given the late onset in patients (mice live 2 years and the disease is evident in humans at middle age), it would remain beneficial for human *in vitro* models to be developed to recapitulate aspects of the human pathology.

Human induced pluripotent stem cells (hiPSCs) have demonstrated utility in human disease modeling since they often capture the disease phenotypes and are amenable to reproducible and large-scale production should that be required for drug screening. In addition, the ability to derive organ-specific cells while retaining the patient’s genetic background and the possibility of generating isogenic controls could allow personalized medicine research and effective drug development[13]. The current study aims to investigate whether in a simple model of vasculature *in vitro,* intrinsic EC defects are evident in patient-derived RVCL-S-hiPSC-ECs using isogenic hiPSCs as a control.

Results and discussion

Generation and CRISPR/Cas9 correction of the hiPSC line from an RVCL-S patient

Skin fibroblasts were obtained from a 52-year-old female RVCL-S patient carrying the most common Val235fs RVCL-S mutation as a result of a single nucleotide insertion (c.703dupG) in the *TREX1* gene (Fig 1A). Fibroblasts were reprogrammed using the Sendai virus to generate the RVCL-$S^{c.703dupG}$ hiPSC line, and three independent clones were characterized. An isogenic hiPSC line was generated by correcting the mutation in the patient hiPSC line using a Cas9-ribonucleoprotein (RNP) complex with a mutation-specific single-guide RNA (sgRNA) and a single-stranded oligodeoxynucleotide (ssODN) donor template. The ssODN donor template contained the wildtype sequence with one additional silent mutation to introduce a novel BsaHI restriction site and disrupt the protospacer adjacent motif (PAM) site (See Table 1 for gRNA and ssODN details). Single cell-derived colonies were screened for repair using the BsaH restriction enzyme of the amplified RVCL-S exon. This resulted in the generation of three independent clones of isogenic genetically-corrected hiPSC; RVCL-S^{corr}. Genomic integrity of the RVCL-S^{corr} clones was confirmed by assessing the copy number of the 24 most commonly altered loci in hiPSCs (Fig S1A). The RVCL-S causing mutation in the parental RVCL-$S^{c.703dupG}$ hiPSC line and the incorporation of the silent mutation was confirmed by Sanger sequencing (Fig 1B). Additional confirmation was done by performing digital droplet PCR (ddPCR) on genomic DNA isolated from a healthy wildtype hiPSC line (LUMC0054iCTRL02), the parental RVCL-$S^{c.703dupG}$ hiPSC line and the three independent clones from the RVCL-S^{corr} hiPSC line using probes that specifically distinguish the wildtype (WT), mutant (MUT) or corrected (Corr) alleles (Fig S1B and C). DdPCR using both the WT and Corr probes showed two separate populations of the WT probe amplitude caused by suboptimal binding to the mutant allele in the RVCL-$S^{c.703dupG}$ hiPSC line with the expected ratio of Corr probe / WT probe for the RVCL-S^{corr} hiPSC clones. A second ddPCR using the WT and Mut probe demonstrated the presence of the Mut allele only in the RVCL-$S^{c.703dupG}$ hiPSC line. In addition, two populations for the WT probe amplitude indicated suboptimal binding of the WT probe also on the corrected allele in the RVCL-S^{corr} hiPSC clones, again confirming proper genetic targeting. The hiPSCs displayed typical stem cell morphology with high nucleus-to-cytoplasm ratio (Fig 1C); normal karyotype was confirmed by G-banding (Fig 1D). The pluripotent status was confirmed by expression and localization of proteins associated with the undifferentiated state: SSEA4, NANOG and OCT3/4 using immunofluorescence staining (Fig 1F). The differentiation potential of the lines was confirmed in a short-term *in vitro* differentiation assay and subsequent immunofluorescence staining for markers associated with the three germ layers: NESTIN and PAX6 (ectoderm), FOXA2 and GATA4 (endoderm), Brachyury (T), CDX2 and Vimentin (mesoderm) (Fig 1E).

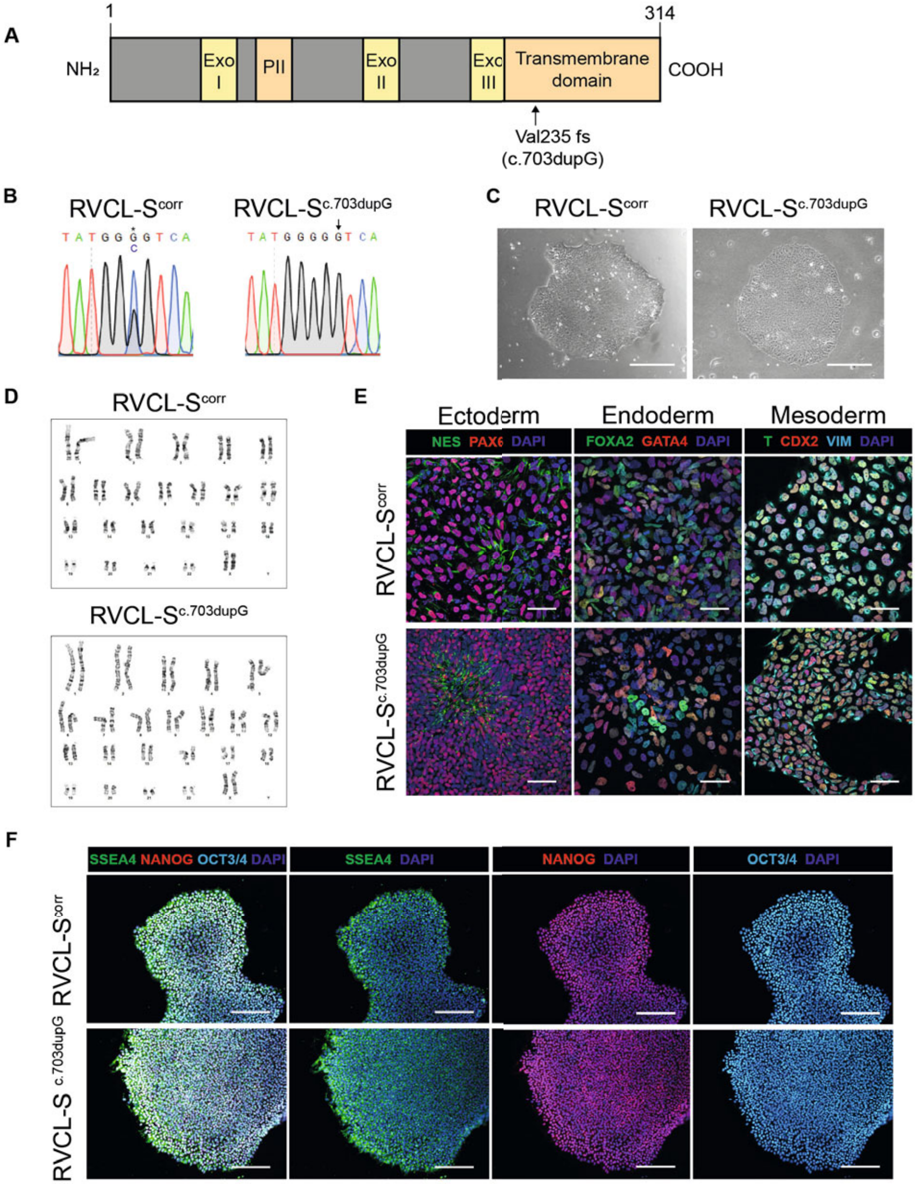

Figure 1. Generation and characterization of RVCL-S patient hiPSC line and CRISPR/Cas9 corrected isogenic control. (A) Schematic overview of the TREX1 protein with its exonuclease domains (Exo), proline II motif (PII) and transmembrane domain with the most common Val235fs RVCL-S causing mutation shown. **(B)** Sanger sequencing of genomic DNA isolated from corrected and mutant hiPSC clones confirming repair of the TREX1 mutation (arrow) and the introduction of a silent mutation (c.701G>C) (asterisk) that creates a new restriction site for BsaHI. **(C)** Representative brightfield images showing hiPSC colony morphology. Scale bars: 250 µm. **(D)** Representative karyograms (G-banding) of corrected and mutant hiPSC clones. **(E)** Immunofluorescent images of the short term differentiation demonstrating derivatives of the three germ layers: NES and PAX6 (ectoderm), FOXA2 and GATA4 (endoderm), Brachyury (T), CDX2 and Vimentin (VIM) (mesoderm). Scale bars: 50 µm. **(F)** Immunofluorescent images of expression of markers of the undifferentiated state: SSEA4 (green), NANOG (red) and OCT3/4 (cyan). Nuclei stained with DAPI (blue). Scale bars: 200 µm.

Over the last several years it has been noted that female hiPSC lines may have differences in X-chromosome inactivation (XCI) status. XCI is a dosage compensation mechanism enabling similar expression of X-linked genes in XY males and XX females[14]. Aberrant XCI states, as defined by the change from an inactivated X-chromosome to an eroded X-chromosome, could potentially shift hiPSCs to a more malignant phenotype with upregulation of oncogenes and deceased differentiation potential *in vivo*[15,16]. In addition, it has been shown that erosion of human XCI in *in vitro* cultures could result in major changes in dosage compensation leading to alterations in the total protein content in hiPSCs[17]. To ensure that results in hiPSC-derivatives are comparable, we assessed the XCI status of RVCL-S hiPSC clones. We included three previously characterized lines[18] as controls: an eroded female line (hESC line H9 purchased from the WiCell institute), a male line (LUMC0072iCTRL01) and a female line with normal XCI status (LUMC0099iCTRL04). Expression of the main initiator of X-chromosome inactivation, long non-coding RNA *XIST*, showed differences in expression between clones (Fig S2A). RVCL-S^{corr} Clone 1 and RVCL-S$^{c.703dupG}$ Clone 2 had the highest expression, similar to the control hiPSC line with the normal XCI status. In addition, we analyzed the presence of 'repressive' mark H3K27me3[19] on the X-chromosome by immunofluorescence staining (Fig S2B and C). This confirmed the variability between XCI status of lines and clones. Because of the discrepancy between the clones, we decided to continue with one clone for both RVCL-S-lines to ensure comparable dosage compensation between the lines, and thus potentially, a more comparable differentiation potential. Therefore, all remaining experiments were performed with three independent differentiations from RVCL-S^{corr} Clone 1 and RVCL-S$^{c.703dupG}$ Clone 2 that was used as a parental clone for CRISPR/Cas9 correction.

Generation of RVCL-S-hiPSC-ECs

Since RVCL-S pathologies have been linked to EC dysfunction[2,9], we differentiated hiPSCs into ECs using a previously described protocol[20,21]. CD31$^+$ hiPSC-ECs were isolated at day 10 of differentiation, expanded for one passage and finally cryopreserved until use. RVCL-S^{corr} and RVCL-S$^{c.703dupG}$ hiPSC-ECs showed typical EC morphology (Fig 2A). Fluorescence-activated cell sorting (FACS) analysis demonstrated a similar percentage of CD31, vascular endothelial cadherin (VEC) double-positive cells, indicating comparable differentiation efficiency (Fig 2B and C). In addition, these CD31 VEC double-positive hiPSC-ECs showed no differences in expression of EC-specific surface markers, such as vascular endothelial growth factor receptor (VEGFR2/KDR), VEGFR3 (/FLT4), Endoglin (ENG or CD105) and C-X-C chemokine receptor type 4 (CXCR4/CD184) (Fig 2B and C). Additionally, immunofluorescence staining confirmed the presence and proper localization of EC-associated markers VEC, CD31 and vWF (Fig 2D). Notably, immunofluorescence staining for the same markers in hiPSC-ECs from all RVCL-S^{corr} and RVCL-S$^{c.703dupG}$ clones demonstrated a reduced expression in clones 2 and 3 of RVCL-S^{corr} (Fig S3A). This was confirmed by expression at the RNA level using RNA sequencing (Fig S3B). This might relate to the reduced XCI observed in these clones, something which was also confirmed at the RNA level in hiPSC-ECs (Fig S3E), similar to the previous observation in the undifferentiated hiPSC. This hypothesis is, however, not fully supported by the high expression of EC-markers by RVCL-S$^{c.703dupG}$ Clone 3, which also showed a lower expression of XIST and an lower percentage of H3K27me3 staining. Hence a more in-depth analysis is needed to further elucidate differences between the generated clones.

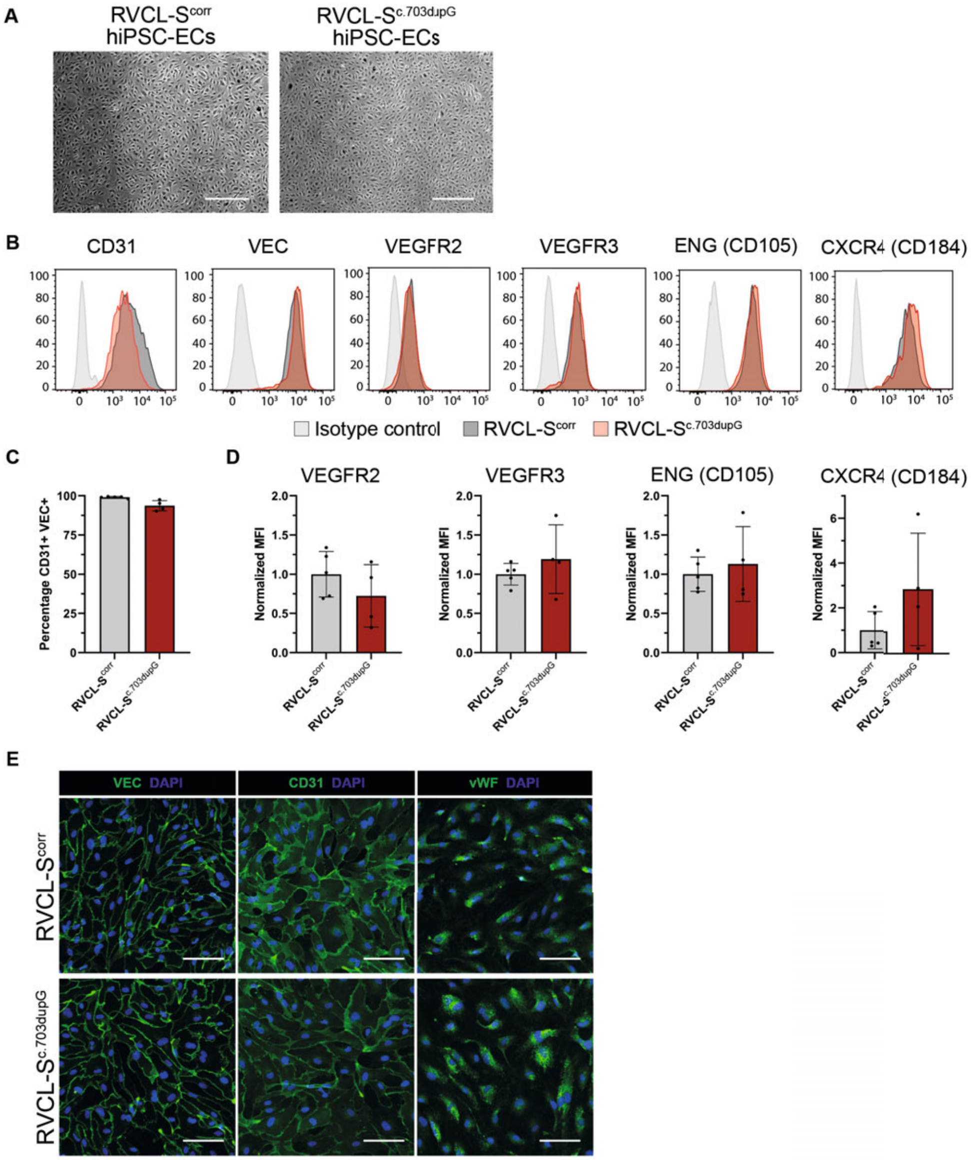

Figure 2. Characterization of RVCL-S-hiPSC-ECs. (A) Representative brightfield images showing typical EC morphology of hiPSC-ECs. Scale bars: 500 µm. **(B)** Representative histograms of fluorescence-activated cell sorting (FACS) analysis of EC surface marker expression on isolated RVCL-S^{corr} and RVCL-$S^{c.703dupG}$ hiPSC-ECs, and corresponding isotype controls. **(C)** Quantification of percentage of CD31+VEC+ hiPSC-ECs (P2) differentiated from RVCL-S^{corr} and RVCL-$S^{c.703dupG}$ hiPSCs. N=4 from three independent differentiations. **(D)** Quantification of relative surface expression of EC markers VEC, CD31, KDR, VEGFR3, CD105 and CXCR4 on hiPSC-ECs (P2) differentiated from RVCL-S^{corr} and RVCL-$S^{c.703dupG}$ hiPSCs. Data are shown as median fluorescent intensity values ± SD and are normalized to RVCL-S^{corr}. N=4 from three independent differentiations. **(E)** Immunofluorescent images of EC markers VEC, CD31 and vWF on hiPSC-ECs (P2) differentiated from RVCL-S^{corr} and RVCL-$S^{c.703dupG}$ hiPSCs. Scale bars: 100 µm.

Functional characterization of RVCL-S-hiPSC-ECs shows no apparent differences

To test the functionality of the RVCL-S^{corr} and RVCL-$S^{c.703dupG}$ hiPSC-ECs, we assessed proliferation and barrier function. Proliferation was investigated by live-cell imaging and quantification by staining of hiPSC-ECs using a nuclear dye and imaging every three hours using an IncuCyte® S3 Live-Cell Analysis System (Fig 3A). Nuclei counts were normalized to a specific time-point per experiment to remove differences in cell seeding density. Low variability in proliferation was observed between differentiation batches within RVCL-S^{corr} (Fig 3B) and RVCL-$S^{c.703dupG}$ (Fig 3C) hiPSC-ECs. Notably, only linear growth was observed, instead of exponential growth. This could be potentially caused by contact inhibition or limited nutrient availability. Follow-up experiments using additional control lines and primary ECs, sensitive to either of these mechanisms should be performed to explain the cause for the difference in proliferation profile for the RVCL-S^{corr} and RVCL-$S^{c.703dupG}$ hiPSC-ECs. Regardless, no differences were observed in proliferation (Fig 3D), quantified as doubling time (Fig 3D and E) between the disease and corrected hiPSC-ECs. Observed doubling times were slightly higher than those observed for primary ECs *in vitro* (12 – 48 hours), and these differences correlated with the lack of exponential growth phase.

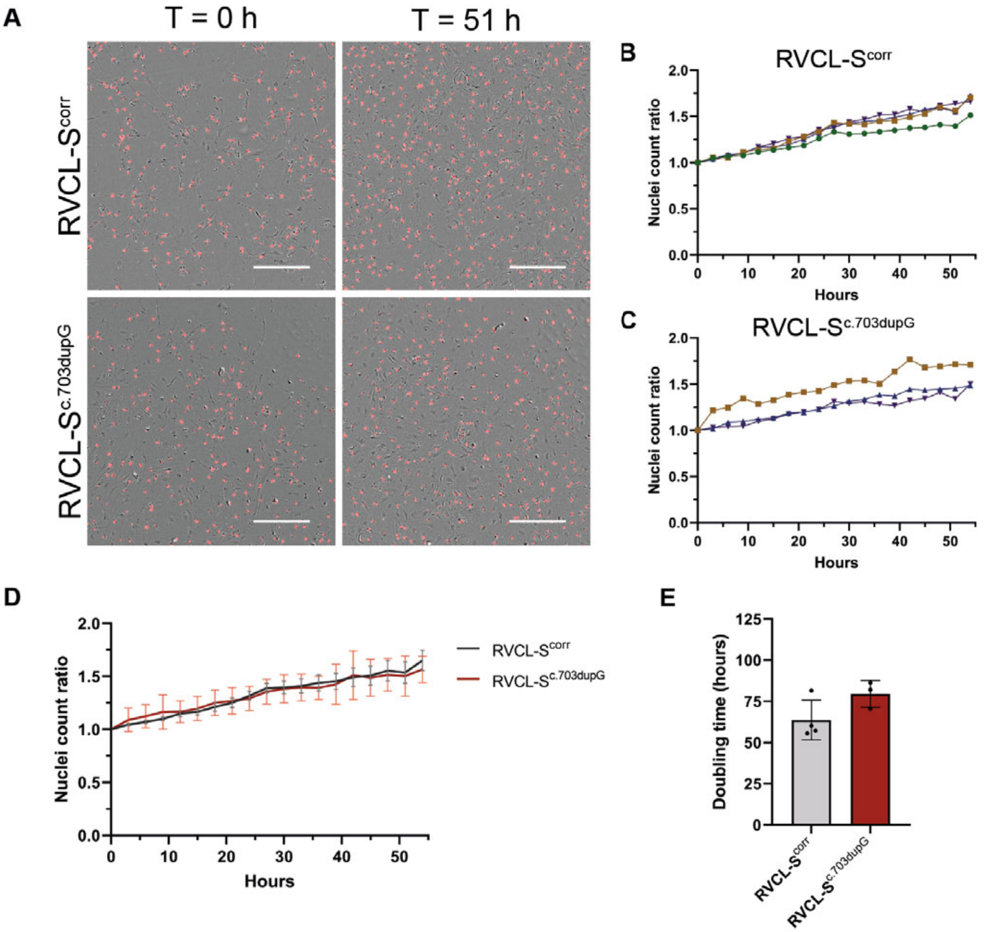

Figure 3. Assessment of proliferation of RVCL-S-hiPSC-ECs. **(A)** Representative overlay image of brightfield and incucyte nuclear identification in proliferation assay at t = 0 h and t = 51 h of RVCL-S$^{\text{corr}}$ and RVCL-S$^{\text{c.703dupG}}$ hiPSC-ECs. Scale bars: 400 µm. **(B)** Normalized nuclear count ratio for proliferation assay with RVCL-S$^{\text{corr}}$ hiPSC-ECs. N=3 from three independent differentiations. **(C)** Normalized nuclear count ratio for proliferation assay with RVCL-S$^{\text{c.703dupG}}$ hiPSC-ECs. N=3 from two independent differentiations. **(D)** Mean normalized nuclear count ratio for proliferation assay with RVCL-S$^{\text{corr}}$ hiPSC-ECs and RVCL-S$^{\text{c.703dupG}}$ hiPSC-ECs. Data are shown as mean values ± SD of N=4 from three independent differentiations for RVCL-S$^{\text{corr}}$ and N=3 from 2 independent differentiations for RVCL-S$^{\text{c.703dupG}}$ hiPSC-ECs. **(E)** Quantification of doubling time for RVCL-S$^{\text{corr}}$ hiPSC-ECs and RVCL-S$^{\text{c.703dupG}}$ hiPSC-ECs. Data are shown as mean values ± SD of N=4 from three independent differentiations for RVCL-S$^{\text{corr}}$,and N=3 from two independent differentiations for RVCL-S$^{\text{c.703dupG}}$ hiPSC-ECs.

Barrier function and EC migration were assessed by real-time impedance spectroscopy using an integrated assay of electrical wound healing as previously described[20]. Both the absolute resistance and migration rates of the RVCL-S$^{\text{corr}}$ hiPSC-EC monolayers had low variability between independent differentiation batches (Fig 4A and E). Higher variability was observed for the same parameters for RVCL-S$^{\text{c.703dupG}}$ hiPSC-EC monolayers (Fig 4B and F).

This was in contrast to previous data which indicated low batch-to-batch variability of CD31$^+$ hiPSC-ECs from two independent lines[20]. Overall, no significant differences were observed in barrier function and EC migration between the RVCL-S^{corr} and RVCL-S$^{c.703dupG}$ hiPSC-ECs (Fig 4C, D, G and H).

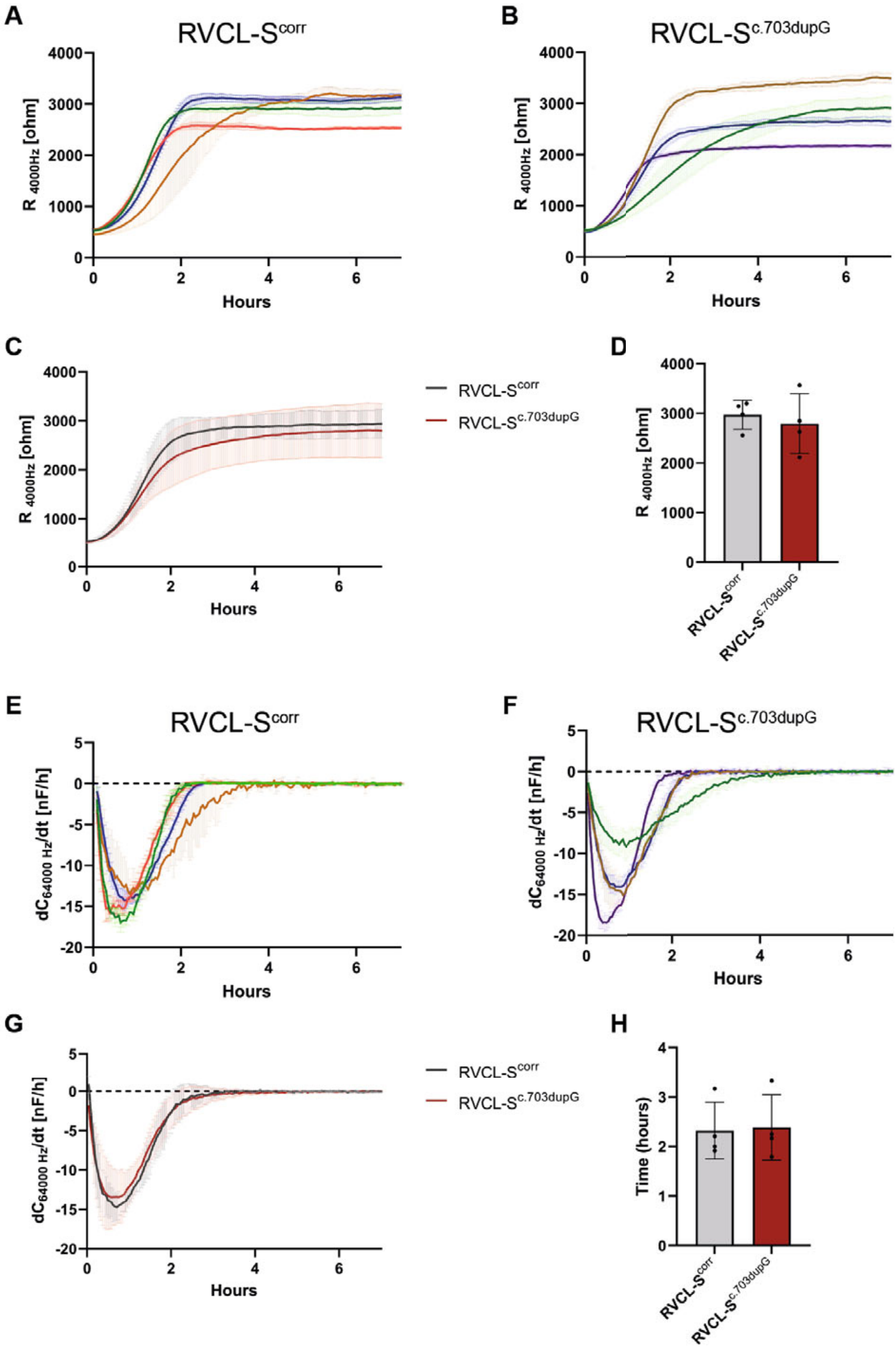

Figure 4. Assessment of barrier function and real-time migration of RVCL-S-hiPSC-ECs. (A) Absolute resistance values at 4000 Hz of RVCL-S^{corr} hiPSC-EC monolayers. Data are shown as mean values ± SD of N=4, each indicated with a different color, from three independent differentiations. **(B)** Absolute resistance values at 4.000 Hz of RVCL-S$^{c.703dupG}$ hiPSC-EC monolayers. Data are shown as mean values ± SD of N=4, each indicated with a different color, from three independent differentiations. **(C)** Mean absolute resistance values at 4000 Hz of RVCL-S^{corr} and RVCL-S$^{c.703dupG}$ hiPSC-EC monolayers. Data are shown as combined mean values ± SD of N=4 from three independent differentiations. **(D)** Quantification of absolute resistance values at 4000 Hz of RVCL-S^{corr} and RVCL-S$^{c.703dupG}$ hiPSC-EC monolayers. Data shown as mean values ± SD of N=4 from three independent differentiations. **(E)** Speed of migration (dC/dt) determined as a change in capacitance at 64000 Hz over time after electrical wound healing for RVCL-S^{corr} hiPSC-ECs. Data are shown as mean values ± SD of N=4, each indicated with a different color, from three independent differentiations. **(F)** Speed of migration (dC/dt) determined as a change in capacitance at 64000 Hz over time after electrical wound healing for RVCL-S$^{c.703dupG}$ hiPSC-ECs. Data are shown as mean values ± SD of N=4, each indicated with a different color, from three independent differentiations. **(G)** Mean speed of migration (dC/dt) determined as a change in capacitance at 64000 Hz over time after electrical wound healing for RVCL-S^{corr} and RVCL-S$^{c.703dupG}$ hiPSC-ECs. Data are shown as combined mean values ± SD of N=4 from three independent differentiations. (H) Quantification of migration rates determined as time upon wound closure DC/dt > (-0.1 nF/h). Data are shown as mean values ± SD of N=4 from three independent differentiations.

Conclusion and future perspective

We generated hiPSC lines from one RVCL-S patient and corrected the mutation using CRISPR/Cas9 to create isogenic genetically-corrected control hiPSC line. We did not examine whether the TREX1 protein expression and localization in these clones had been altered by the disease as in patients due to lack of appropriate antibodies targeting the unaltered N-terminus of the TREX1 protein[1,5]. The lines all differentiated to hiPSC-ECs using our standard protocol. We confirmed the expected genotypes but in a series of simple assays (migration, EC barrier function) we did not find any differences between the diseased and corrected hiPSC-ECs. There may be several reasons for this: (i) the identity of the ECs derived using our protocol did not correspond to those in the tissues manifesting the disease in patients (eye, brain, liver, kidney); (ii) any EC defects only manifest in a more complex model systems; that was previously the case in our study on hereditary hemorrhagic telangiectasia (HHT) where a disease phenotype was only apparent when hiPSC-ECs were included a 3D vessel-on-chip system[22]. An inflammatory component might be required in the model system to induce the phenotype; this could be either stimulating the hiPSC-ECs with pro-inflammatory cytokines or co-culturing them with inflammatory cells.

In summary, we have created isogenic pairs of disease and control RVCL-S-hiPSC-ECs but found no differences between them in basic EC assays *in vitro*. However, these lines can form a basis for future investigation into the mechanisms underlying RVCL-S pathology but likely require more complex modeling and additional disease-promoting microenvironments.

Materials and Methods

hiPSC lines and maintenance

Skin biopsies were taken from a female RVCL-S patient (with informed consent approved by Leiden University Medical Center ethics committee under the P13.080 ‘‘Parapluprotocol: hiPSC.’’) for the generation of the RVCL-S hiPSC line (LUMC0210iTREX). Fibroblasts were isolated from the skin biopsies and cultured in fibroblast medium (FM) composed of DMEM/F12 Glutamax supplemented with 10% Fetal Bovine Serum (FBS), 1% Non-Essential Amino Acids, 0.18% β-mercaptoethanol, 1% penicillin/streptomycin (all from ThermoFisher Scientific: #31331; #10270; #11140 #31350; #15070) and 10 μg/mL Ascorbic acid (Sigma-Aldrich, #A5960). At passage 3, 10^5 cells were transduced with Sendai virus (SeVdp (KOSM302L), MOI 7.5). 16 h after transduction, cells were plated at the density of 10^3 cells/cm^2 on Matrigel coated plates (Corning, #354277) in FM. The next day, cells were refreshed and subsequently maintained with ReproTeSR^{TM} (Stemcell Technologies, #05921, #05922, #05923). At day 18, culture was shifted to TeSRTM E8^{TM} medium (Stemcell Technologies, #05990). After mechanical picking, hiPSCs were maintained in TeSRTM-E8^{TM} on vitronectin-coated plates (Stemcell Technologies, #07180) at 37 °C, 5% CO2 and 20% O_2. HiPSCs were passaged once a week as small aggregates using Gentle Cell Dissociation Reagent (Stemcell Technologies, #07174) with a splitting ratio of 1:25. The following hiPSC lines were used: LUMC0210iTREX (female, reprogrammed from skin fibroblasts using Sendai virus, mutation Val235fs), IsoLUMC0210iTREX02 (CRISPR-Cas9 edited to remove the Val235fs mutation) and LUMC0054iCTRL02 (https://hpscreg.eu/cell-line/LUMCi001-A).

CRISPR-Cas9 mutation correction

For genetic repair, $1*10^5$ LUMC0210iTREX02 cells were electroporated at passage 15 with the Alt-R Cas9-RNP complex and the ssODN (both IDT) using a factory-defined program (program 6) of the Neon Transfection System (Invitrogen). Subsequently, cells were cultured in two Synthemax II-SC (Corning)-coated wells of a 12-well plate in TESR-plus with CloneR2 (Stem Cell Technologies). For single-cell cloning, 1000 cells were plated onto a Synthemax II-SC-coated 10 cm dish in TESR-plus with CloneR2. After 8-12 days, hiPSC colonies were split into two VN-coated wells of a 96-well plate in TESR-plus. The gene region of interest was amplified by PCR using the Terra PCR Direct Polymerase Mix (TaKaRa) from DNA isolated from one well (QuickExtract solution, Lucigen). Successfully edited clones were identified by AatII enzyme (New England Biolabs) activity and confirmed by Sanger sequencing performed by the Leiden Genome Technology Centre (LGTC).

Table 1. Primers, gRNA and ssODN used.

	Target	Forward/Reverse primer (5′-3′)
Correction confirmation (PCR/sequencing)	RVCL-S exon 1	CACACAATGGTGACCGCTACG/TGACCATCCTGCTAGGGAAAGTG
gRNA		ACCATCAGGCCCATGTATGG
ssODN		ACCACAGGCCCTGCTGCGGTGGGTGGATGCTCACGCCAGGCCTTTCGGCACCATCAGGCCCATGTATGGcGTCACAGCCTCTGCTAGGACCAAGCCAAGACCATCTGCTGTCACAACCACTGCACACCTGGCCACAACCA
qPCR primer	hARP	CACCATTGAAATCCTGAGTGATGT/TGACCAGCCCAAAGGAGAAG
qPCR primer	XIST	CAGCATGGTTGGTGACACCTAAG/TGGAATGAGCAGTGTGCGAT

Immunofluorescence staining

HiPSCs at passage 17 for LUMC0210iTREX01, LUMC0210iTREX02 and LUMC0210iTREX03 or passage 24 for Iso1LUMC0210iTREX02, Iso2LUMC0210iTREX02, Iso3LUMC0210iTREX02 were fixed in 2% PFA for 30 min, permeabilized with 0.1% Triton X-100, and blocked with 4% normal swine serum (NSS, DAKO) at room temperature (RT) for 1 h. Primary antibodies were added and incubated overnight at 4°C (See Table 2 for antibodies used). After washing, secondary antibodies were added for 1 h at RT. Nuclei were stained with DAPI, and coverslips were mounted using Mowiol (Merck Millipore). Images were acquired on a Leica TCS SP8 microscope or an EVOS M7000 microscope (ThermoFisher Scientific). For quantification of H3K27me3, cells (n>1000 cells per cell line) were imaged by generating a maximum intensity projection (MIP) from a z-stack using an EVOS M7000 microscope. Subsequently, the MIP was used to manually count cells positive for the H3K27me3 marker.

Table 2. List of antibodies used.

Antibody	Species	Use	Source	Dilution	Catalog #
OCT3/4-BV421	Mouse	FACS	BD Biosciences	1:25	565644
NANOG-PE	Mouse	FACS	BD Biosciences	1:5	560483
SSEA4-FITC	Mouse	FACS	Miltenyi Biotec	1:25	130-098-371
OCT3/4	Mouse	IF	Santa Cruz	1:100	sc-5279
NANOG	Mouse	IF	Santa Cruz	1:150	sc-293121
SSEA4	Mouse	IF	BioLegend	1:30	330402
Nestin-Alexa488	Mouse	IF	Cell Signaling Technology	1:200	60433
PAX6-Alexa647	Rabbit	IF	Cell Signaling Technology	1:200	60433
FOXA2-Alexa555	Rabbit	IF	Cell Signaling Technology	1:500	8186
GATA4-Alexa647	Rabbit	IF	Cell Signaling Technology	1:200	36966
Brachyury-Alexa488	Rabbit	IF	Cell Signaling Technology	1:200	81694
Vimentin-Alexa647	Rabbit	IF	Cell Signaling Technology	1:300	5741
VEC	Rabbit	IF	Cell Signaling Technology	1:300	2158
CD31	Mouse	IF	Agilent Dako	1:300	M0823
vWF	Rabbit	IF	Agilent Dako	1:200	A0082

FACS staining

HiPSCs were dissociated at passage 15 with TrypLE for 5 min at 37°C. Samples were fixed for 15 min in 200 µL of Reagent A of the fix & perm kit (ThermoFisher Scientific). Cells were washed once in FACS buffer (PBS without Ca^{2+} and Mg^{2+} with 0.5% BSA and 2 mM EDTA), resuspended in 80 µL of Reagent B with conjugated antibodies (Table 2) and incubated in the dark for 60 min at RT. Subsequently, samples were washed once and resuspended in FACS buffer before being measured on the MACSQuant VYB flow cytometer (Miltenyi Biotec). Analysis was performed using FlowJo v.10.6.1 software.

In vitro trilineage differentiation

The ability of hiPSCs to differentiate into the three germ layers (ectoderm, mesoderm, and endoderm) was assessed using differentiation with a Trilineage differentiation kit (Stem Cell Technologies). Differentiation was done according to the manufacturer's instructions on hESC-qualified Matrigel (Corning) coated coverslips. After 5 to 7 days of culture cells were fixed using 2% PFA.

Karyotype analysis

HiPSCs at passage 9 were karyotyped by Cell Guidance systems (UK) and a total of 20 metaphases were counted.

RNA isolation and quantitative RT-PCR

RNA was extracted from hiPSC-ECs monolayers using the NucleoSpin RNA XS kit (Macherey-Nagel) and cDNA was synthesized using an iScript-cDNA Synthesis kit (Bio-Rad). ITaq Universal SYBR Green Supermixes (Bio-Rad) and Bio-Rad CFX384 real-time system were used for the PCR reaction and detection. CDNA from three lines was added as controls, namely eroded female (hESC line H9 purchased from the WiCell institute), male (LUMC0072iCTRL01), and female with normal XCI status (LUMC0099iCTRL04)[18]. Primers used can be found in Table 1. Relative gene expression was calculated using the ΔCt method and normalized to housekeeping gene hARP.

RNA Sequencing

RNA was isolated and purified using the NucleoSpin RNA-kit (Macherey-Nagel). RNA-sequencing and whole-genome transcriptome data were generated by Novogene (UK) on the Illumina NovaSeq6000 platform, paired-end sequencing and read length of 150bp with a sequencing depth of 20M raw reads per sample.

Raw RNA-seq reads were processed using the open-source BIOWDL RNAseq pipeline v5.0.0 developed at the LUMC. The pipeline performs FASTQ preprocessing (including quality control, quality trimming, and adapter clipping), RNA-Seq alignment, read quantification, and optionally transcript assembly. FastQC was used for checking raw read QC. Adapter clipping was performed using Cutadapt (v2.4) with default settings. RNA-Seq reads' alignment was performed using STAR (v2.7.5a) on GRCh38 human reference genome. Gene read quantification was performed using featureCounts (v2.0.1) with the setting "-M -O --fraction". Gene annotation used for quantification was Ensembl version 105. Count tables were normalized using EdgeR[23], and genes were filtered based on their expression across all the samples according to previous publication[23].

Proliferation Assay

HiPSC-ECs were seeded on bovine fibronectin (Sigma, F1141, 20 µg/mL) coated 96 well plates (Greiner, 655160) at a density of 9.375 K/cm2 (= 3K/well) in EGM-2 culture medium (PromoCell) supplemented with 1:2000 IncuCyte NucLight Rapid Red Reagent (Sartorius, Cat# 4717). Plates were left undisturbed at RT for 1 h to allow cell attachment before placing them in the IncuCyte® S3 Live-Cell Analysis System. Wells were imaged every 3 h with a 4X objective in the red channel (excitation 567-607 nm, emission 622-704 nm) with an acquisition time of 500 ms. Images were analyzed using the built-in Incucyte analysis software to extract cell count per well over time. Data was extracted and plotted using

GraphPad Prism 9 software. Doubling time was calculated by first fitting a linear regression curve on the data and extracting the slope using Graphpad Prism 9 software. To determine the doubling time from this linear part of the curve, the following formula was used: doubling time = ln(2) / (growth rate), in which the growth rate is the slope of the fitted linear regression.

Endothelial barrier function analysis

Endothelial barrier function and real-time migration analysis was performed using electric cell-substrate impedance sensing (ECIS Zθ, Applied Biophysics) as described previously[20]. In brief, CD31+ hiPSC-ECs were seeded on fibronectin-coated (50 µg/mL) ECIS arrays (8W10E PET, Applied Biophysics) at a density of ~50,000 cells/cm^2 and left undisturbed at RT for 2h to allow cell attachment. For barrier function and migration studies, cells were left for at least 6h to establish a confluent monolayer before refreshing half of the medium with fresh EGM-2. One hour after medium change, the electric wound (10 sec pulse of 5000 µA at 60 kHz) was applied. Recovery of the barrier was monitored over the next 12h. Multiple frequency/time (MFT) mode was used for real-time assessment of the barrier and monolayer confluence. The absolute resistance values at 4000 Hz were quantified by taking the mean of 6h of stable absolute resistance after wound closure. Quantification of migration rates was determined as a time upon closing the wound DC/dt > (-0.1 nF/h).

Droplet digital PCR (ddPCR)

DdPCR experiments were performed and analyzed using a Q200 AutoDG thermocycler (Bio-Rad), a QX200 Droplet Digital PCR System (Bio-Rad) and QuantaSoft software (Bio-Rad). DdPCR assays comprised premixtures of a primer pair (18 µM each) and a FAM- or HEX-conjugated hydrolysis probe (5 µM). Details regarding the assays are listed in Table 3. Reactions (22 µL) were prepared using 2X ddPCR Supermix for Probes (no dUTP, Bio-Rad), 900 nM of each primer, 250 nM of the probe, 30 ng of gDNA and 2-5 U of HindIII (NEB). Automated droplet generation, PCR amplification procedure and analysis were all performed following the manufacturer’s instructions.

WT/Cor and WT/Mut assays

Probes were designed to specifically distinguish the WT allele (HEX-conjugated) over the Corrected and Mutant alleles (FAM-conjugated). Locked nucleic acids were used to reduce the length of the probes, thereby increasing their specificity (See Table 3).

iCS-digital™ PSC 24-probes assay

The genome integrity was assessed using the iCS-digital™ PSC 24-probes kit (Stemgenomics) following the manufacturer’s instructions.

Table 3. Primer-Probe sets used for ddPCR assays.

Name	Sequence (5'-3')	Fluorophore-Quencher
TREX1_Primer_Fwd	TCAGCATCTGTCAGTGGAGA	-
TREX1_Primer_Rev	GTGACAGCAGATGGTCTTG	-
TREX1_Probe_Cor	ATG G+C+G +TC+A C+AG C	FAM-ZEN-IBFQ
TREX1_Probe_Mut	ATG GG+G +G+T+C ACA G	FAM-ZEN-IBFQ
TREX1_Probe_WT	ATG GG+G +T+C+A CAG C	HEX-ZEN-IBFQ

+ symbol indicates the next nucleotide is a locked nucleic acid

Acknowledgements

We thank N. Nakanishi (National Institute of Advanced Industrial Science and Technology, Japan) for providing SeV and the Laboratorium voor Diagnostische Genoom Analyse (LGDA, LUMC) for karyotype analysis. We thank Yolanda Chang and Susana M. Chuva de Sousa Lopes for discussion on XCI, trial of the XIST antibody and providing cDNA for the XIST RT-PCR controls. This work was supported by The Netherlands Organ-on-Chip Initiative, an NWO Gravitation project funded by the Ministry of Education, Culture and Science of the government of the Netherlands (024.003.001) and the Novo Nordisk Foundation Center for Stem Cell Medicine, supported by Novo Nordisk Foundation grants (NNF21CC0073729).

Author Contributions

Conceptualization, G.M.T. and V.V.O.; methodology, D.M.N., D.G.K. and V.V.O.; investigation, D.M.N., D.G.K., F.E.v.d.H., M.J.B., A.B. and R.W.J.v.H.; visualization, D.M.N.; resources, C.L.M., A.M.J.M.v.d.M and V.V.O.; writing – original draft, D.M.N., D.G.K., A.M.J.M.v.d.M and V.V.O; writing – review & editing, D.M.N., D.G.K., C.L.M. and V.V.O.; supervision, C.F., C.L.M. and V.V.O.; project administration, V.V.O.; funding acquisition, C.L.M. and V.V.O.

Conflict of interest

The authors declare no competing interests.

References

1. Richards, A. et al. C-terminal truncations in human 3′-5′ DNA exonuclease TREX1 cause autosomal dominant retinal vasculopathy with cerebral leukodystrophy. Nat Genet 39, 1068–1070 (2007).
2. Stam, A. H. et al. Retinal vasculopathy with cerebral leukoencephalopathy and systemic manifestations. Brain 139, 2909–2922 (2016).
3. Wilms, A. E., de Boer, I. & Terwindt, G. M. Retinal Vasculopathy with Cerebral Leukoen cephalopathy and Systemic manifestations (RVCL-S): An update on basic science and clini cal perspectives. Cereb Circ Cogn Behav 3, 100046 (2022).
4. DiFrancesco, J. C. et al. TREX1 C-terminal frameshift mutations in the systemic variant of retinal vasculopathy with cerebral leukodystrophy. Neurological Sciences 36, 323–330 (2015).
5. Hasan, M. et al. Cytosolic Nuclease TREX1 Regulates Oligosaccharyltransferase Activity Independent of Nuclease Activity to Suppress Immune Activation. Immunity 43, 463–474 (2015).
6. Kothari, P. H. et al. TREX1 is expressed by microglia in normal human brain and increases in regions affected by ischemia. Brain Pathology 1–16 (2018) doi:10.1111/bpa.12626.
7. Saito, R. et al. Retinal vasculopathy with cerebral leukodystrophy: Clinicopathologic fea tures of an autopsied patient with a heterozygous TREX 1 mutation. J Neuropathol Exp Neurol 78, 181–186 (2019).
8. Kolar, G. R. et al. Neuropathology and genetics of cerebroretinal vasculopathies. Brain Pathol 24, 510–518 (2014).
9. de Boer, I. et al. RVCL-S and CADASIL display distinct impaired vascular function. Neurology 91, e956–e963 (2018).
10. Pelzer, N. et al. Circulating Endothelial Markers in Retinal Vasculopathy With Cerebral Leu koencephalopathy and Systemic Manifestations. Stroke (2017) doi:10.1161/STROKEA HA.117.018556.
11. Sakai, T. et al. DNase-active TREX1 frame-shift mutants induce serologic autoimmunity in mice. J Autoimmun. 31, 872–881 (2017).
12. Mulder, I. A. et al. Increased Mortality and Vascular Phenotype in a Knock- In Mouse Model of Retinal Vasculopathy With Cerebral Leukoencephalopathy and Systemic Manifestations. Stroke 1–8 (2020) doi:10.1161/STROKEAHA.119.025176.
13. Passier, R., Orlova, V. V. & Mummery, C. L. Complex Tissue and Disease Modeling using hiPSCs. Cell Stem Cell 18, 309–321 (2016).
14. Loda, A., Collombet, S. & Heard, E. Gene regulation in time and space during X-chromo some inactivation. Nat Rev Mol Cell Biol 23, 231–249 (2022).
15. Anguera, M. C. et al. Molecular signatures of human induced pluripotent stem cells high light sex differences and cancer genes. Cell Stem Cell 11, 75–90 (2012).
16. Geens, M. & Chuva De Sousa Lopes, S. M. X chromosome inactivation in human pluripotent stem cells as a model for human development: back to the drawing board? Hum Reprod Update 23, 520–532 (2017).
17. Brenes, A. J. et al. Erosion of human X chromosome inactivation causes major remodeling of the iPSC proteome. Cell Rep 35, (2021).
18. Chang, Y. W. et al. Tissue of origin, but not XCI state, influences germ cell differentiation from human pluripotent stem cells. Cells 10, (2021).

19. Patrat, C., Ouimette, J. F. & Rougeulle, C. X chromosome inactivation in human develop ment. Development (Cambridge) vol. 147 Preprint at https://doi.org/10.1242/dev.183095 (2020).
20. Halaidych, O. V. et al. Inflammatory Responses and Barrier Function of Endothelial Cells Derived from Human Induced Pluripotent Stem Cells. Stem Cell Reports 10, 1642–1656 (2018).
21. Orlova, V. V. et al. Generation, expansion and functional analysis of endothelial cells and pericytes derived from human pluripotent stem cells. Nat Protoc 9, 1514–1531 (2014).
22. Orlova, V. V. et al. Vascular defects associated with hereditary hemorrhagic telangiectasia revealed in patient-derived isogenic iPSCs in 3D vessels on chip. Stem Cell Reports 17, 1536–1545 (2022).
23. Chen, Y., Lun, A. T. L. & Smyth, G. K. From reads to genes to pathways: differential ex pression analysis of RNA-Seq experiments using Rsubread and the edgeR quasi-likelihood pipeline. F1000Res 5, 1438 (2016).

Supplementary Material

Contents
Supplemental Figures:

Figure S1. Related to Figure 1. Assessment of genomic stability and correct CRISPR-Cas9 editing in RVCL-S hiPSCs.

Figure S2. Related to Figure 1. Assessment of X-chromosome inactivation status in RVCL-S hiPSCs.

Figure S3. Related to Figure 2. Immunofluorescence staining and RNA expression of EC markers in RVCL-S hiPSC-ECs.

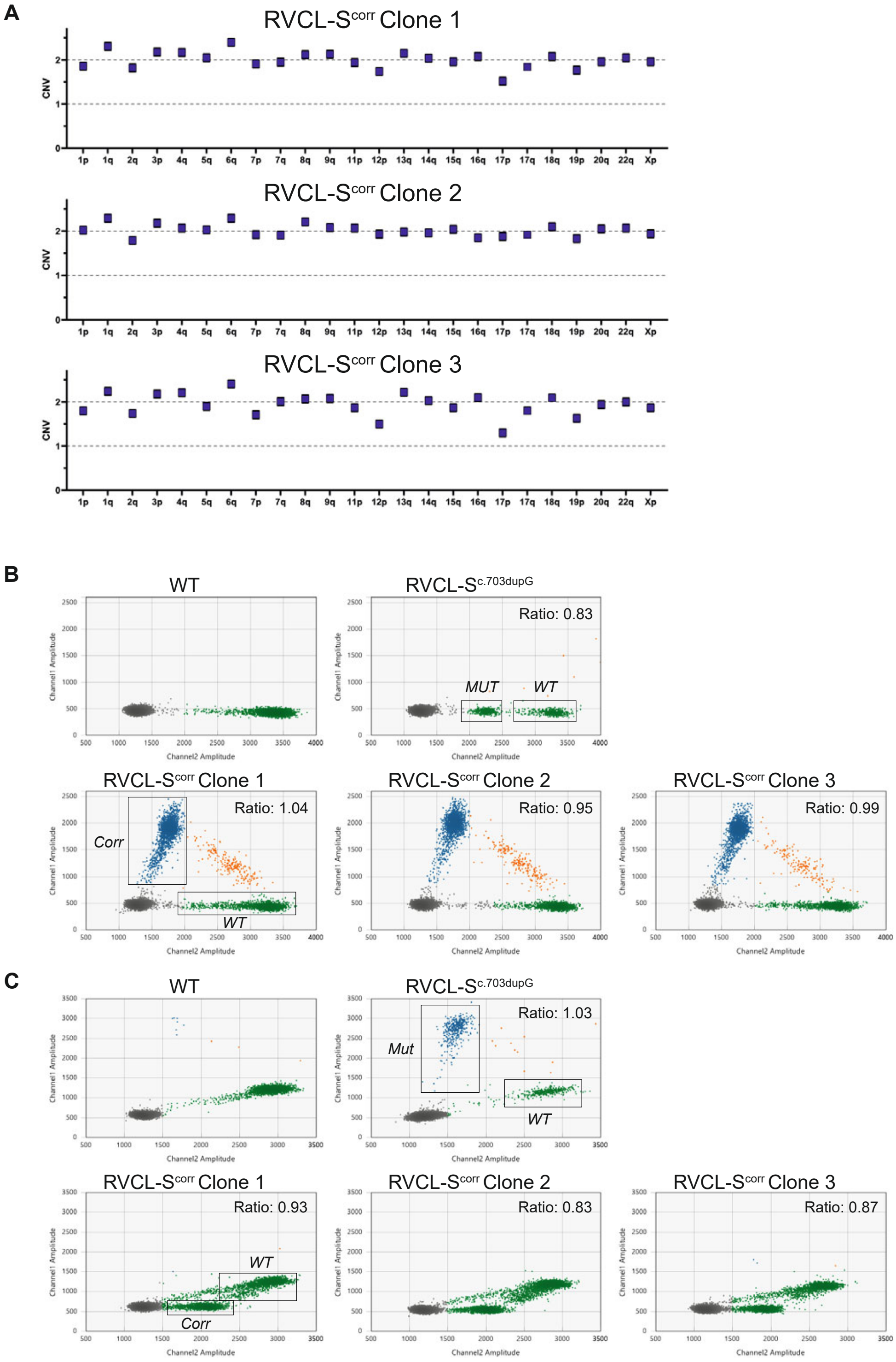
A
RVCL-Scorr Clone 1
RVCL-Scorr Clone 2
RVCL-Scorr Clone 3
CNV
0
1
2
1p 1q 2q 3p 4q 5q 6q 7p 7q 8q 9q 11p 12p 13q 14q 15q 16q 17p 17q 18q 19p 20q 22q Xp
B
WT
RVCL-Sc.703dupG
Ratio: 0.83
MUT
WT
RVCL-Scorr Clone 1
Ratio: 1.04
Corr
WT
RVCL-Scorr Clone 2
Ratio: 0.95
RVCL-Scorr Clone 3
Ratio: 0.99
Channel1 Amplitude
Channel2 Amplitude
C
WT
RVCL-Sc.703dupG
Ratio: 1.03
Mut
WT
RVCL-Scorr Clone 1
Ratio: 0.93
WT
Corr
RVCL-Scorr Clone 2
Ratio: 0.83
RVCL-Scorr Clone 3
Ratio: 0.87
Channel1 Amplitude
Channel2 Amplitude

Figure S1: Assessment of genomic stability and correct CRISPR-Cas9 editing in RVCL-S hiPSCs. (A) DdPCR examining genomic integrity of the RVCL-S^{corr} hiPSC clones by determining the copy number variation (CNV) of the 24 genomic locations that consist of 92% of the most recurrent genomic abnormalities in hPSCs. **(B)** DdPCR dot plots demonstrating the presence of the wildtype (WT), Mutant (MUT) or Corrected (Corr) allele. Genomic DNA of the WT hiPSC line, the parental RVCL-S$^{c.703dupG}$ hiPSC line and the three clones of the RVCL-S^{corr} hiPSC line were investigated. Dots represent droplets containing the Corr sequence on channel 1 and the WT sequence on channel 2. Suboptimal binding of the WT probe on the MUT allele results in a separate population in the RVCL-S$^{c.703dupG}$ plot. In the RVCL-S$^{c.703dupG}$ plot, the ratio between the MUT population and WT population is displayed. In the RVCL-S^{corr} clones plots, the ratio between the Corr population and WT population is displayed. **(C)** DdPCR dot plots demonstrating the presence of the wildtype (WT), Mutant (MUT) or Corrected (Corr) allele. Genomic DNA of the WT hiPSC line, the parental RVCL-S$^{c.703dupG}$ hiPSC line and the three clones of the RVCL-S^{corr} hiPSC line were investigated. Dots represent droplets containing the Mut sequence on channel 1 and the WT sequence on channel 2. Suboptimal binding of the WT probe on the Corr allele results in a separate population in the RVCL-S^{corr} clones plots. In the RVCL-S^{corr} clones plots, the ratio between the Corr population and WT population is shown.

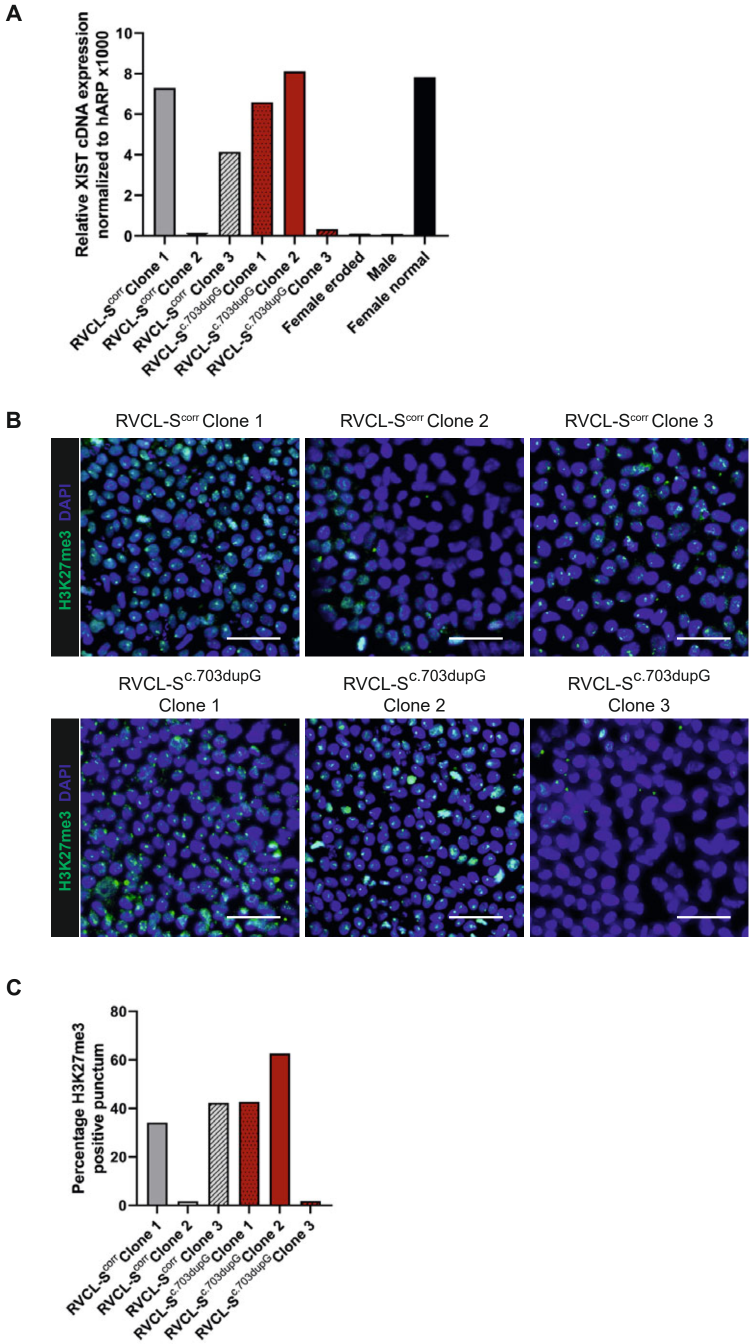

Figure S2. Assessment of X-chromosome inactivation status in RVCL-S hiPSCs. (A) Gene expression, as assessed by RT-qPCR, of XIST for the three clones of both RVCL-S$^{\text{corr}}$ and RVCL-S$^{\text{c.703dupG}}$ hiPSCs. **(B)** Representative immunofluorescence staining for H3K27me3 for the three clones of both RVCL-S$^{\text{corr}}$ and RVCL-S$^{\text{c.703dupG}}$ hiPSCs. **(C)** Quantification of H3K27me3 positive cells (percentage). N> 1000 cells per clone quantified.

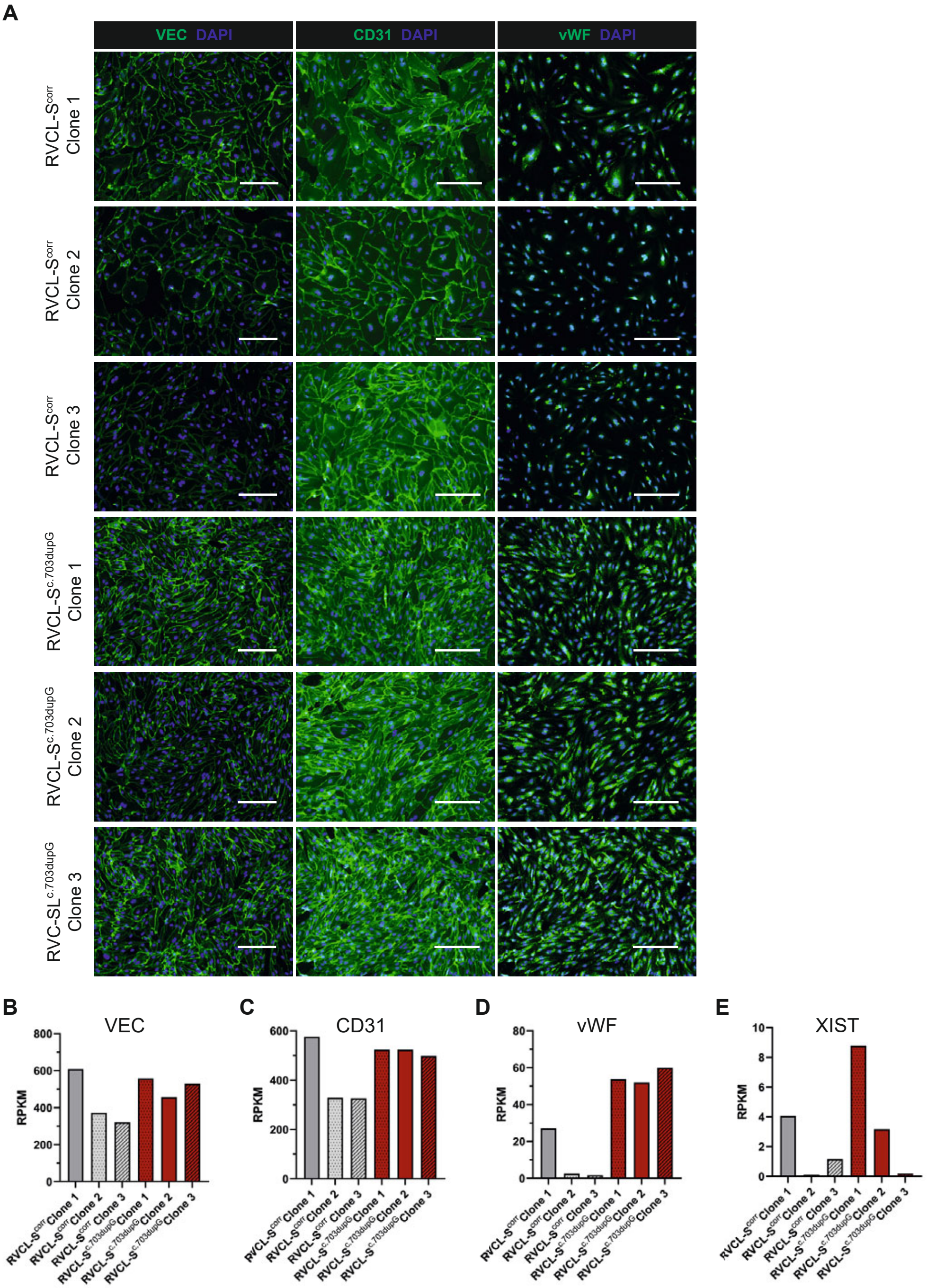

Figure S3. Immunofluorescence staining and RNA expression of EC markers in RVCL-S hiPSC-ECs. (A) Immunofluorescence staining of EC markers VEC, CD31 and vWF of RVCL-S^{corr} and RVCL-S$^{c.703dupG}$ hiPSC-ECs. Scale bars: 100 µm. **(B-E)** Gene expression, as assessed by RNA sequencing, for EC-markers VEC (B), CD31 (C), vWF (D) and XIST (E).